ADVANCED FUNCTIONAL MATERIALS
www.afm-journal.de

A GFET Nitrile Sensor Using a Graphene-Binding Fusion Protein

Abubaker A. Mohamed, Hironaga Noguchi, Mirano Tsukiiwa, Chen Chen, Rachel S. Heath, M. Qadri E. Mubarak, Takumi Komikawa, Masayoshi Tanaka, Mina Okochi, Sam P. de Visser, Yuhei Hayamizu,* and Christopher F. Blanford**

A new route to single-step and non-covalent immobilization of proteins on graphene is exemplified with the first biosensor for nitriles based on a graphene field-effect transistor (GFET). The biological recognition element is a fusion protein consisting of nitrile reductase QueF from *Escherichia coli* with an N-terminal self-assembling and graphene-binding dodecapeptide. Atomic force microscopy and analysis using a quartz crystal microbalance show that both the oligopeptide and the fusion protein incorporating it form a single adlayer of monomeric enzyme on graphene. The fusion protein has a 6.3-fold increase in binding affinity for benzyl cyanide (BnCN) versus wild-type QueF and a 1.4-fold increase for affinity for the enzyme's natural substrate preQ$_0$. Density functional theory analysis of QueF's catalytic cycle with BnCN shows similar transition-state barriers to preQ$_0$, but differences in the formation of the initial thioimidate covalent bonding ($\Delta G^{\ddagger}$ = 19.0 kcal mol^{-1} for preQ$_0$ vs 27.7 kcal mol^{-1} for BnCN) and final disassociation step (ΔG = −24.3 kcal mol^{-1} for preQ$_0$ vs ΔG = +4.6 kcal mol^{-1} for BnCN). Not only do these results offer a single-step route to GFET modification, but they also present new opportunities in the biocatalytic synthesis of primary amines from nitriles.

1. Introduction

The emerging field of bioelectronics has helped integrate electronic circuits into biological systems and provide an analytical tool for assessing physiological[1] and pharmaceutical biomarkers.[2] Graphene field effect transistors (GFETs) are of particular interest because they exploit the material properties of graphene such as its high surface/volume ratio, high charge carrier mobility,[3] and its thermal and mechanical resistance to create a surface capable of transducing a biological binding event via a specific recognition element, such as a protein, into an electrical output.[4] GFETs have been used to create low-noise, high-sensitivity biosensors capable of performing low-voltage operation.[5,6] GFETs have been employed in health monitoring with wearable and implantable devices,[6] environmental,[7] and biochemical sensing [8,9] including SARS-CoV-2 detection.[10,11]

Traditional nitrile detection was done via an alcohol-mediated reduction of nitrile to amine followed by precipitation and dry mass weighing.[12] Current methods of organic nitrile detection uses surface-enhanced Raman scattering,[13] gas chromatography,[14,15] electrochemical,[16] and colorimetric analysis.[17] However, most of these methods either do not translate well to into the field or lack the sensitivity required.

The development of a sensor capable of accurate and rapid detection of nitriles would be an important tool in agriculture.

A. A. Mohamed, C. F. Blanford
Department of Materials
University of Manchester
Oxford Road, Manchester M13 9PL, UK
E-mail: christopher.blanford@manchester.ac.uk

A. A. Mohamed, R. S. Heath, M. Q. E. Mubarak, S. P. de Visser, C. F. Blanford
Manchester Institute of Biotechnology
University of Manchester
131 Princess Street, Manchester M1 7DN, UK
E-mail: sam.devisser@manchester.ac.uk

The ORCID identification number(s) for the author(s) of this article can be found under https://doi.org/10.1002/adfm.202207669.

© 2022 The Authors. Advanced Functional Materials published by Wiley-VCH GmbH. This is an open access article under the terms of the Creative Commons Attribution License, which permits use, distribution and reproduction in any medium, provided the original work is properly cited.

DOI: 10.1002/adfm.202207669

H. Noguchi, M. Tsukiiwa, C. Chen, Y. Hayamizu
Department of Materials Science and Engineering
Tokyo Institute of Technology
2-12-1 Ōokayama, Meguro-ku, Tokyo 152–8550, Japan
E-mail: hayamizu.y.aa@m.titech.ac.jp

R. S. Heath
Department of Chemistry
University of Manchester
Oxford Road, Manchester M13 9PL, UK

M. Q. E. Mubarak, S. P. de Visser
Department of Chemical Engineering
University of Manchester
Oxford Road, Manchester M13 9PL, UK

T. Komikawa, M. Tanaka, M. Okochi
Department of Chemical Science and Engineering
Tokyo Institute of Technology
2-12-1 Ōokayama, Meguro-ku, Tokyo 152–8552, Japan

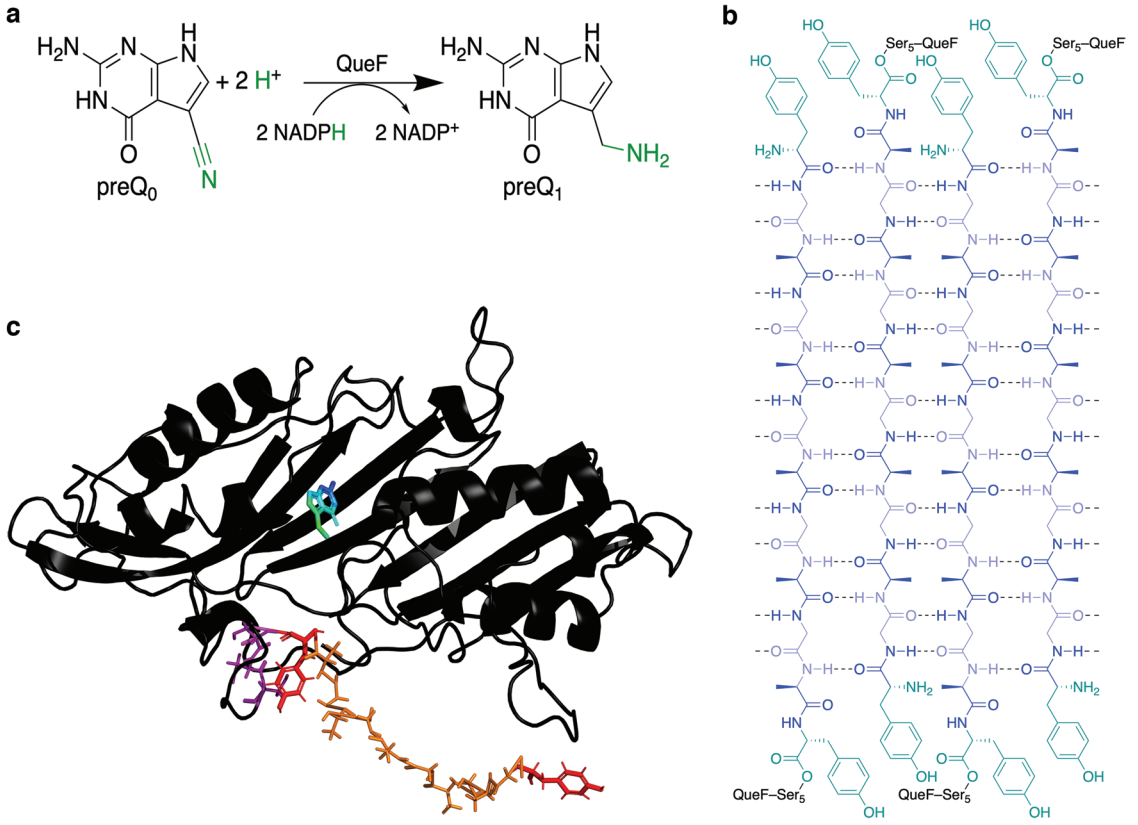

Figure 1. a) The natural reaction of QueF in vivo.[22] b) Schematic representation of an antiparallel β-sheet formation of the Y5Y fusion protein. c) Homology model of preQ0 (green sticks) docked in QueF (black ribbon) with a short serine linker (pink) added followed by the Y5Y chain (red). Model created using PDB 4GHM and I-TASSER.[36]

Volatile nitriles are produced from glucosinolates, predominately found in brassicas, when under herbivore attack.[18] Benzyl cyanide (BnCN) is a useful proof-of-concept compound for agricultural biosensors because they would be able to detect the plants' natural distress signals to recruit parasitoid species as a secondary defense mechanism.[19] Nitrile emissions can be used to alert farmers of pest location and allow site-specific pesticide administration, which in turn would lower pesticide usage.[20] Additionally, nitriles are ubiquitous in industry, such as in the production of textile fibers, synthetic rubbers, and thermoplastic resins;[21] a nitrile sensor would be useful for environmental monitoring.

QueF nitrile reductase was chosen as a proof-of-concept biological recognition element because it can catalyze the four-electron reduction of nitrile functional groups to amines. QueF is the only enzyme known to carry out the reduction of a nitrile to a primary amine by a two-step reaction involving hydride transfer from two NADPH molecules.[22] Its natural function is the four-electron reducing the nitrile group of 7-cyano-7-deazaguanine ($preQ_0$) to 7-aminomethyl-7-deazaguanine ($preQ_1$) (**Figure 1**a).[22]

One of the bottlenecks for enzyme-based GFET devices is the protein immobilization method used. Non-specific adsorption of protein on graphene can produce false positive/negative signals as the entry of target analytes to the enzyme's active site is obstructed that therefore decreases the sensing capabilities of the GFET.[23] Conventional covalently mediated immobilization techniques allow for stronger protein attachment methods than non-covalent binding,[4] but also disrupt the electronic structure of graphene and take place preferentially near defects and grain boundaries,[24] affecting the sensitivity of the GFET sensor device. Therefore, non-covalent GFET functionalization is preferred in order to preserve graphenes sp^2 arrangement and consequent high carrier mobility required for high-sensitivity measurements.[25] This is often done by using a 1-pyrenebutanoic acid *N*-hydroxysuccinimide ester (PBASE) conjugate because the pyrene moiety has strong affinity toward the basal plane of graphene via π–π stacking,[26] while the esterified end reacts with terminal amines in biological recognition agents like antibodies to form stable amide bonds.[9,24] However, PBASE can bind to any surface amine group,[27] which can move the recognition element's binding site away from the surface, attach the proteins in a more than one orientation, and decrease analyte accessibility.

Here, we present a non-covalent enzyme immobilization technique. We engineered a wild-type QueF to include a bifunctional self-assembling and graphene-binding oligopeptide to act as an anchor for directed immobilization. The affinity tag's sequence, YGAGAGAGAGAY (Y5Y, Figure 1b), is based on the silk protein fibroin.[28,29] The glycine–alanine (GA) repeat unit forms a stable antiparallel β-sheet structure via hydrogen bonds among the amide bonds to other GA domains. Y5Y forms mono-molecular self-assembled structures ordering with three-fold symmetry on graphene,[30] where the two flanking tyrosine

© 2022 The Authors. Advanced Functional Materials published by Wiley-VCH GmbH

residues are responsible for forming non-covalent attachment to graphene via π–π interaction. These kinds of self-assembled peptides revealed their ability to connect biological molecules with 2D nanomaterials[31,32] and they were used as a molecular scaffold for the immobilization of biological recognition elements on GFETs.[33,34]

The Y5Y tag was engineered as an extension to the N-terminus of the nitrile reductase QueF (Figure 1c) via PCR (Table S1, Supporting Information) and homologously expressed in *E. coli*. An additional triple serine linker domain was added between the Y5Y and QueF domain to allow for increased flexibility. QueF's active site is located at the interface of two monomers and its substrate specificity is believed to be modulated, in part, by its dimeric conformation.[35] Adding a graphene-binding segment to the protein was hypothesized to favor the formation of the monomer form on the surface and thereby increase solvent accessibility to the active site.

The high selectivity of QueF to its natural substrate has been reported[22] and so to explain the observed GFET response to BnCN, a complete density functional theory (DFT) model was constructed. QueF mechanism of action is composed of four main reaction stages (**RS**): 1) formation of a thioamide bond through a C—S covalent bond between the nitrile group of the substrate and a cysteine residue, 2) donation of a hydride from NADPH to the carbon forming the thioamide bond, 3) cleavage of the C—S covalent bond and formation of an imine intermediate, and 4) transfer of a hydride ion from a second NADPH molecule to the imine intermediate (**Figure 2**).[37] The charge around the active site differs in three of the four intermediates, which could be translated into a change in source-drain current (i_{sd}) from GFET:[25] **RS-1** to **RS-2** takes two protons from the solvent, and the **RS-2** to **RS-3**, and **RS-4** to **RS-1** steps both release $NADP^+$.

2. Results and Discussion

2.1. QueF-Functionalized Graphene Field Effect Transistor (GFET)

Figure 3 shows how the drain current, i_{sd}, of GFET sensors modified with either the QueF–Y5Y fusion protein or QueF wild-type (QueF WT) responds to the enzymes' natural substrate, $preQ_0$, and the target nitrile BnCN. The magnitude of the response increases with increasing nitrile concentration and can be modeled as a protein–ligand binding equilibrium (**Table 1**). QueF-Y5Y shows a strong response upon binding to both nitriles but with opposing i_{sd} response whereas QueF-WT functionalized surface showed a low response comparable to bare graphene controls (Figure S2, Supporting Information) indicating enhanced enzyme binding capabilities mediated by the Y5Y tag.

The limit of detection (LoD) was calculated from the point at which the 95% prediction band no longer crossed $y = 1$. For QueF-Y5Y, the LoD is ≈0.35 µM for BnCN and ≈10 nM for $preQ_0$, consistent with the less specific interaction between BnCN and the enzyme. The response is $(8.9 \pm 2.4) \times 10^{-4}$ nM^{-1} for BnCN and $(-55.2 \pm 6.9) \times 10^{-4}$ nM^{-1} for $preQ_0$ when then analyte concentration equals K_d.

Adding additional NADPH had no effect on sensor response to $preQ_0$, suggesting that NADPH depletion did not limit the reaction rate. For BnCN reaction with the QueF-Y5Y

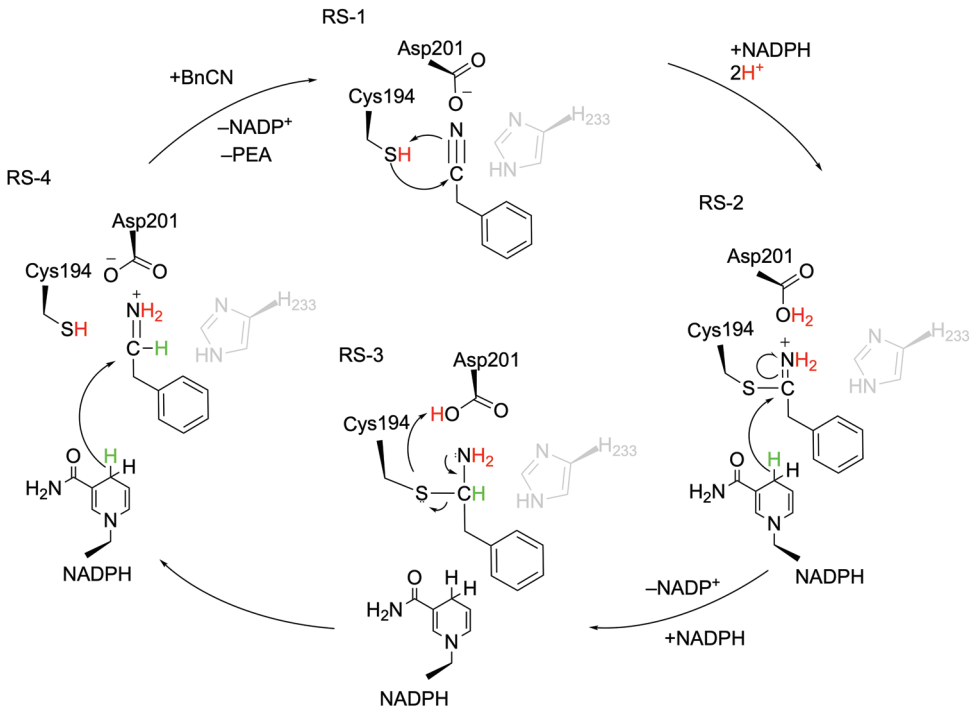

Figure 2. Reaction scheme for the four main steps of enzymatic reduction of benzyl cyanide (BnCN) to phenylethylamine (PEA) by QueF studied by DFT.[37] Hydrides transferred from NADPH are shown in green and protons from the solvent are shown in red.

© 2022 The Authors. Advanced Functional Materials published by Wiley-VCH GmbH

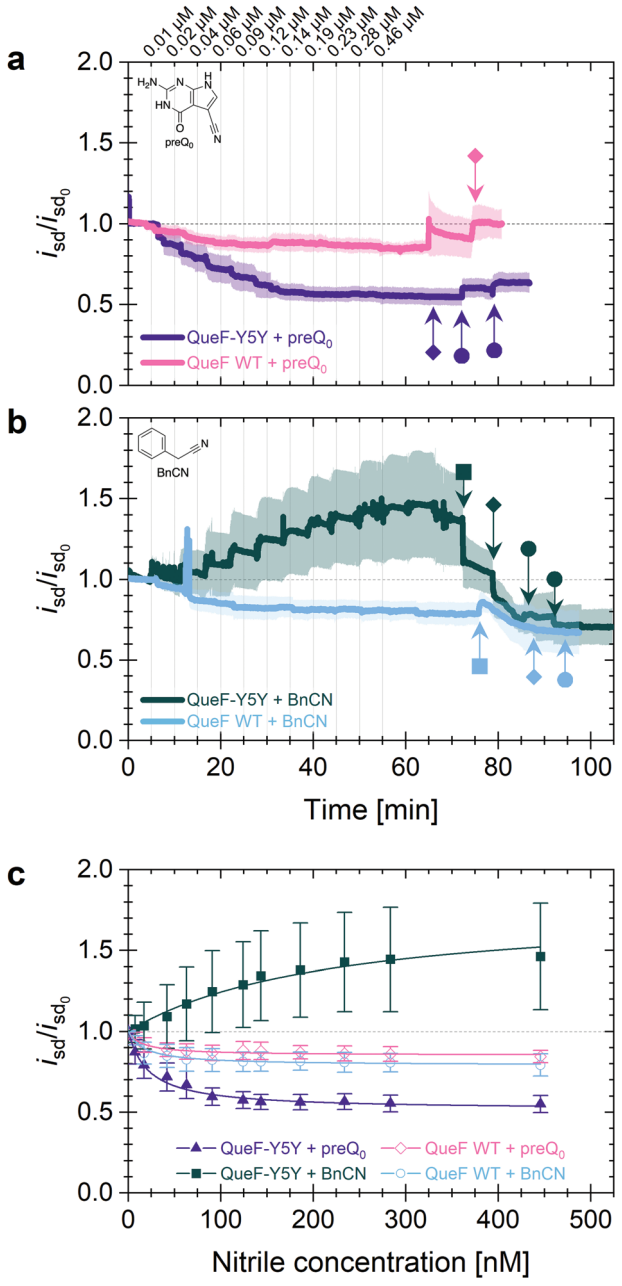

Figure 3. Response of enzyme-functionalized GFETs to two nitriles. Normalized response of wild-type QueF and QueF-Y5Y fusion protein to concentrations of a) $preQ_0$ and b) benzyl cyanide (BnCN) to 500 nM. Gray vertical lines represent approximate timings for analyte addition. Arrowed symbols: ● = sensor wash in phosphate buffer, ◆ = addition of 4 μM NADPH, ■ = addition of 1 M substrate. c) Normalized response curve fittings for each sample. Error bars ranges are mean ± standard deviation. Number of replicates are given in Table 1. Standard deviation in panel c) is calculated from the pooled variance of all signals over 1 min. GFET conditions: V_g: mV, V_d: 5 mV.

functionalized surface, there is a large decrease in response after NADPH addition, but only after 1 M BnCN had been added to the GFET.

The polarity and amplitude of the GFET signal depend on the gate voltage (V_g) relative to the charge neutral point (CNP). For QueF-Y5Y samples, $preQ_0$ shows *p*–type doping as the CNP increases that can be attributed in part to the reduction of the nitrile to amine while BnCN shows an opposite trend except at a potentially denaturing 1 M concentration (Figure S3, Supporting Information).

2.2. Reaction Energy Profile

GFET responses are sensitive to changes in charges near the surface. The reaction stages of QueF have three different charges so the dominant or terminal stage of the reaction may differ between the two nitriles. We applied DFT to compare the size of energy barriers for QueF's interactions with $preQ_0$ and BnCN to determine thermodynamically stable stages and intermediates.

The first stage is the activation of the Cys194 via proton transfer to the Asp201 and covalent bond formation between Cys194 and substrate (Figure S11, Supporting Information). Both substrates show a stable intermediate complex (–12.8 and –14.2 kcal mol^{-1} for $preQ_0$ and BnCN, respectively, **Figure 4**).

In the second stage of the catalytic cycle the first hydride transfer takes place from NADPH to the nitrile group of the substrate (Figure S12, Supporting Information) with barriers of 24.0 kcal mol^{-1} for BnCN and 19.1 kcal mol^{-1} for $preQ_0$. The driving force and kinetics for this step appears not be dependent on the substrate. In this step there is signification change in charge as the Asp201 and the thioimidate gains a proton from the environment[37] giving the model zero charge.

The third step is followed by covalent bond cleavage between the protein and substrate (Figure S13, Supporting Information) and reprotonation of Asp201. The third stage requires less driving force for BnCN than $preQ_0$ (–4.6 and –24.3 kcal mol^{-1} respectively) and is less exergonic suggesting that this stage is rapid and likely irreversible for $preQ_0$ but may be in equilibrium for BnCN. The fourth and final stage shows similar mechanism to the first hydride transfer (Figure S14, Supporting Information), which is also the rate-limiting step.

Substrate dissociation seems to be in equilibrium for BnCN and not $preQ_0$, which may explain the disparity in i_{sd} observed between $preQ_0$ and BnCN. In the case of $preQ_0$, the surface charge remains balanced because the $2H^+$ taken from the solvent is given back in the form of the $preQ_1$ amine product whereas in BnCN the product remains in the active site causing a charge disparity between the graphene surface and solvent. This charge disparity can be used to explain the shift in i_{sd}. For BnCN, an increase in i_{sd} is seen, indicating a positive shift in CNP because of positively charged doping attributed to the $2H^+$ taken from the environment. For $preQ_0$ an opposite trend is observed and that can be attributed to the dissociation of the positively charged $preQ_1$ amine and the subsequent hydride transfer in RS-4.

Inhibition of substrate dissociation would also mean BnCN cycle does not undergo RS-4 that would cause a further discrepancy in i_{sd}. Charge imbalances caused by protein catalysis enhances the effective detection of the GFET via changes in charge carriers and leading to a detectable change in i_{sd}. Enzyme selectivity was probed further by immobilizing RGA-GAGARC (R3RC) peptide that is a bifunctional self-assembling, graphene-binding tag with a free cysteine end (Figure S7, Supporting Information) however there was no significant i_{sd}

© 2022 The Authors. Advanced Functional Materials published by Wiley-VCH GmbH

Table 1. Fitting parameters for GFET nitrile sensor responses. Uncertainty values represent standard error of the fit to equation 1. $\Delta R_{sd}(\infty)$ is the maximum GFET response to nitrile addition relative to the no analyte, K_d is the disassociation constant (both determined by Equation 1), and n is the number of channels sampled on a device.

Sensing Element	Nitrile	$\Delta R_{sd}(\infty)$	K_d [nM]	n
QueF-Y5Y	BnCN	$+0.78 \pm 0.10$	218 ± 51	6
QueF-WT	BnCN	-0.211 ± 0.006	17.8 ± 2.3	6
bare graphene	BnCN	$+0.020 \pm 0.007$	0.00 ± 0.19	6
QueF-Y5Y	$preQ_0$	-0.486 ± 0.009	22.0 ± 2.7	7
QueF-WT	$preQ_0$	-0.149 ± 0.006	15.2 ± 3.7	3
bare graphene	$preQ_0$	-0.88 ± 0.35	841 ± 485	5

response upon BnCN addition indicating that the catalysis/binding requires enzyme mediated reaction and not cysteine-nitrile interaction only.

2.3. Surface and Solution Quaternary Structure

In solution QueF monomer resembles two connected ferredoxin-like domains that assemble into dimers[39] or tetramers with the active sites at the interface of two monomer domains.[40] The quaternary structure as well as the composition of amino acids lining the active site create a topohydrophobic core to form a solvent excluded active site to prevent sequestering of the unstable imine intermediates.[35]

AFM analysis shows QueF immobilizing as a monomer rather than the dimer form observed crystallographically (Figure S4, Supporting Information). The active site is at the interface between two domains, so being in the monomer form likely increases solvent accessibility to the active site and allow entry for a wider substrate scope to interact with the catalytic triad of the proteins active site but may cause unexpected by-products.

Protein mass spectrometry of combinations of QueF, the two nitriles, and NADPH (**Figure 5**) shows that QueF forms a 1:1 stoichiometric complex with its natural $preQ_0$ substrate in the absence of NADPH, suggesting all the protein molecules have formed a stable intermediate. The addition of NADPH causes the original protein signal to reappear. The presence of a higher-mass adduct also appears that could be attributed to a protein species with multiple NADPH or $preQ_0$ molecules stably bound. The species is unknown but may be caused by interaction with the $preQ_1$ amine product interaction allosterically.

For mixtures of QueF with BnCN, the most abundant species indicate no bound substrate however there is a low abundance of species with a mass shift equivalent to roughly 30 BnCN molecules bound per QueF, indicating allosteric binding. The addition of NADPH dissociates all the bound BnCN in a similar manner observed with $preQ_0$-bound species. The exact binding position of BnCN is unknown but binding to the active site is probable because the Cys-His-Asp catalytic triad in QueF is known to have strong affinity to nitriles (e.g., cysteine proteases).[41,42]

The mass spectrometry results suggest that QueF monomers react with substrates. In contrast, dimers in low abundance (4 monomer:1 dimer) are observed only in the absence of any nitrile substrates (Figure S5a, Supporting Information). We conclude that upon substrate association/interaction, QueF favors being in the monomer form even in the presence of the NADPH co-factor. Static light scattering analysis showed tetramer formation in the absence of substrates (Figure S6, Supporting Information) indicating substrate induced conformation change for QueF.

Molecular dynamics simulations were perfored to obtain binding dynamics of monomer QueF variants binding to graphene surface (Figure S10, Supporting Information). The free energy landscape shows that upon binding to graphene, the QueF does not denature, based on its stable radius of gyration and RMSD; the Y5Y tag remains very flexible.

Measurements with a quartz crystal microbalance with dissipation monitoring (QCM-D), which shows how adlayers form and evolve with ≈1 s resolution,[43] were used to strength our hypotheses about the interactions between the proteins and graphene. Adsorption kinetics were followed by adding QueF-Y5Y and QueF WT to QCM-D resonators coated with CVD graphene (**Figure 6**a).

The binding orientation was deduced from estimates of the areal mass density based on two proposed surface orientations. The crystal structure of a QueF monomer (PDB: 4GHM) shows $3.7 \times 6.6 \times 3.2$ nm dimensions that translates to a theoretical monomer binding density of 299 ng cm^{-2} when the long axis is parallel to the surface. QCM-D mass binding analysis suggests that QueF-Y5Y takes roughly 2 h to form stable layer of QueF monomer (Figure 6a) and this areal mass density correlates to a thickness of ≈2.2 nm that suggest monomer conformation and aligns with AFM analysis done on exfoliated graphene (Figure S4, Supporting Information). QueF-WT likely binds as a multilayer because the adsorbed mass is too high to suggest binding as either a monomer or a dimer. QCM measures the wet mass of adsorbed proteins that can increase the estimated mass,[44] and the packing of the protein on the surface will be less than its maximum, both of which would lower the estimated mass and may explain the initial adsorbed mass of QueF-WT. However, after ≈8 h, QueF-WT appears to change its surface orientation to match QueF-Y5Y (Figure S8, Supporting Information). QueF-Y5Y, in contrast, appears stably bound for at least 12 h. Both enzymes are stably bound to graphene and do not wash off.

Figure 6b presents a d–f[45] plot of both absorption profiles. The mass increase (i.e., frequency decrease) when QueF-WT binds does not include a corresponding increase in dissipation, suggesting the formation of a rigid, probably denatured,

© 2022 The Authors. Advanced Functional Materials published by Wiley-VCH GmbH

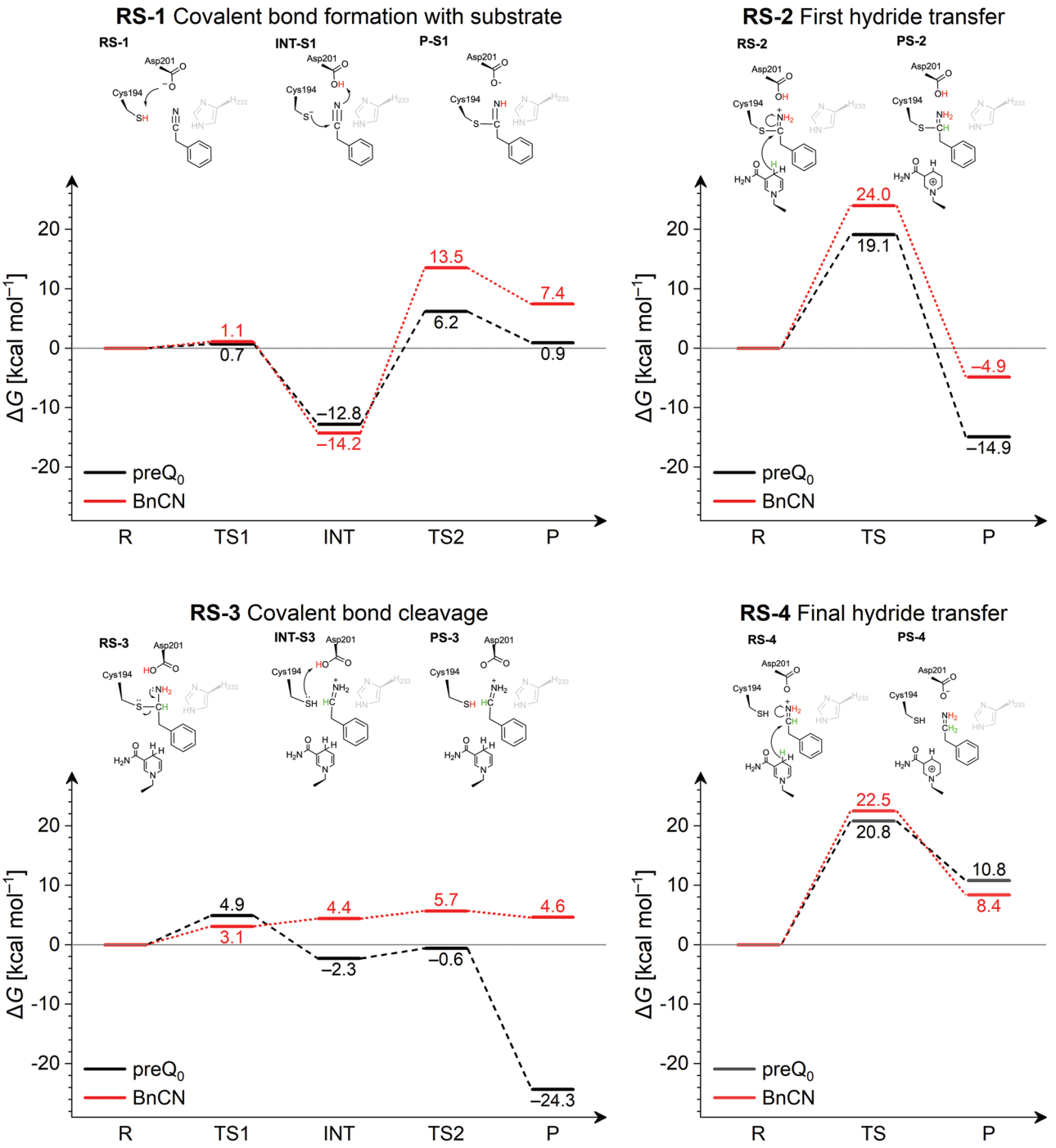

Figure 4. Energy profiles calculated by DFT for the four stages of QueF reduction of its natural substrate preQ$_0$ compared to the target nitrile BnCN. The rate-limiting step is the final hydride transfer. Data for preQ$_0$ from Hirao et al.[38]

adlayer. QCM was used to determine binding conformation of the enzyme variants and shown the enzyme is tightly bound and resistant to washing (Figure S8, Supporting Information).

2.4. Future Work

The release rate of BnCN from infected brassicas has so far only been presented as relative concentrations, but volatile releases of ≈0.1 µM cm^{-2} of leaf area are typical over 24 h following insect infestation.[46] Converting this value into a local concentration requires assumptions about vapor diffusion and convection near the leaf surface and the amount of leaf area under attack, but the detection of nanomolar concentrations is plausible. This study did not examine the effect of possible interferences or selectivity of GFETs using QueF-Y5Y, but these measurements would be essential to translate this research into practice.

© 2022 The Authors. Advanced Functional Materials published by Wiley-VCH GmbH

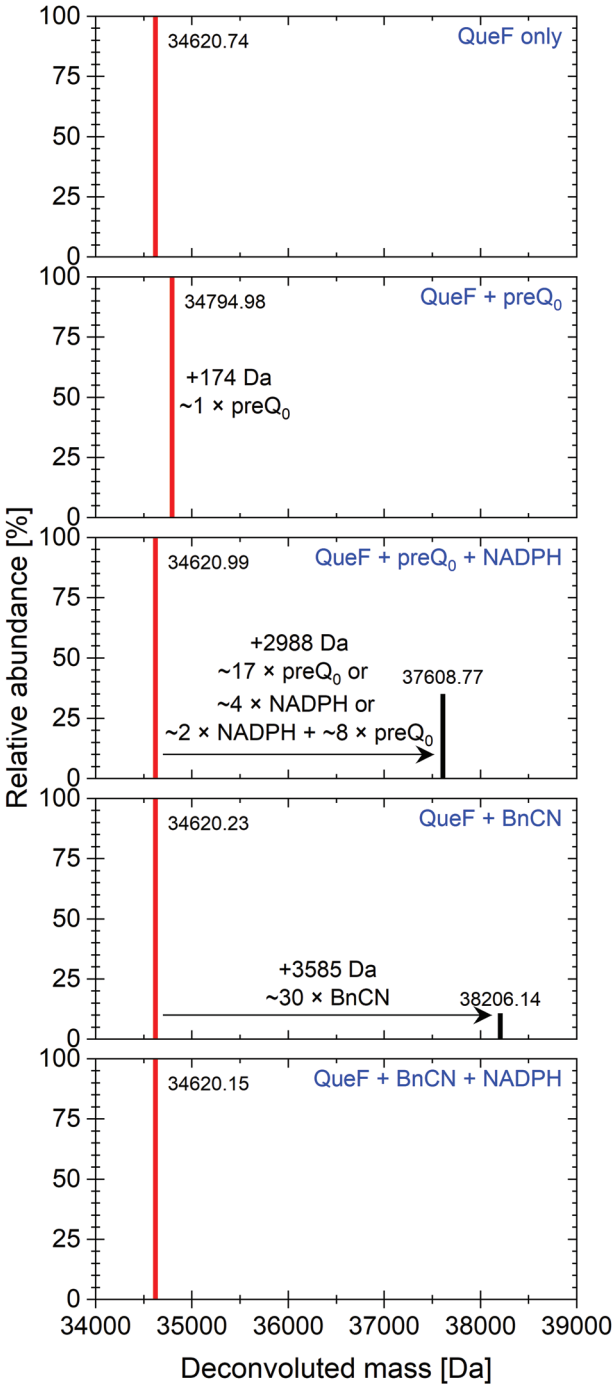

Figure 5. Deconvoluted intact protein mass spectra of QueF WT in the presence or absence of a nitrile, NADPH, or both. Relative abundance of each species is shown for various masses. The QueF monomer has a mass of ca. 34 kDa. Dimer formation is observed in the sample containing only QueF (Figure S5a, Supporting Information). Source spectra are given in Figure S5b–f (Supporting Information).

V_g was held close to the CNP for maximum transconductance and the substrate doping could have shifted V_g toward the CNP.[25,47] This shift may have occurred with $preQ_0$, consistent with the GFET's low response after 135 nM substrate addition. While V_g was held at 500 mV for consistency, the LoD therefore could be increased by optimizing V_g for the specific nitrile to be detected.

QCM results suggest the active lifetime of a sensor is at least 12 h, but the sensors' lifetime in storage and in service still need to be tested. The sensors are likely to be single use because of the strong binding of nitriles to the recognition element.

More generally, incorporating the binding moiety into the recognition element removes the need for surface modification or capping unreacted NHS esters.

3. Conclusions

Standard molecular biology techniques offer a route to single-step non-covalent attachment of proteins to graphene by adding a dodecapeptide graphene-binding moiety to the protein's N terminus: graphene surface modification is not necessary to attach a biological recognition element. The immobilized QueF nitrile reductase, which has a limited substrate scope in solution, can bind to other nitriles. Protein mass spectrometry also indicates that QueF can interact with both nitriles. This expanded substrate scope may link to a switch from a multimeric form in solution to surface-bound protein monomers, which therefore increased active site exposure and accessibility. Static light scattering shows QueF is stable in solution at 25 °C for at least 3 days. QCM shows stable binding of QueF onto graphene with a stabilization period of ≈2 h. DFT analysis shows similar energy barriers between QueF's natural substrate and BnCN except for dissociation step of BnCN. The BnCN disassociation step is in a thermodynamic equilibrium whereas for $preQ_0$ there a highly exothermic and likely irreversible disassociation of the substrate after the first hydride transfers. Changes in thermodynamic steps may explain the disparity observed in i_{sd} sensor response.

4. Experimental Section

Protein Synthesis: The QueF-Y5Y fusion protein was synthesized via PCR with the Y5Y chain being incorporated into the N-terminus of QueF-Y5Y. QueF-Y5Y was then transformed into *E. coli* BL21 cells, cultured, and purified by affinity chromatography. SDS-PAGE showed a single band consistent with a 34 kDa monomer size.

Intact Protein Mass Spectrometry: Porous R2 beads (100 µL) was transferred to a clean Telos tube and washed with 100 µL of 0.1% formic acid in acetonitrile followed by 100 µL of 0.1% formic acid in water. QueF sample was then acidified with 0.1% formic acid and 10 µL of sample was slowly passed through the Telos tube. Sample was then washed twice with 100 µL of 0.1% formic acid in water. Protein was eluted with 20 µL of 0.1% formic acid in 50% acetonitrile (50/50 mixture of 0.1% formic acid in water and 0.1% formic acid in acetonitrile). Eluted protein was then transferred to a low volume injection vial. The run was carried out using Orbitrap Elite mass spectrometry system with Nano source and a Nano U3000 chromatography system (configured for flow injection analysis). Data was analyzed using Protein Deconvolution Software v4 (Thermo Scientific)

Atomic Force Microscopy: Protein conjugates and peptides were measured by atomic force microscopy (Asylum AMFP-3D-SA-J, Asylum Cypher, JP). Graphite (Asbury Carbons, USA) was mechanically exfoliated using adhesive tape and spread across the tape surface. The graphite flakes were transferred to a separate piece of adhesive tape. This process was repeated twice to reduce the layers of the graphite flake. The final

© 2022 The Authors. Advanced Functional Materials published by Wiley-VCH GmbH

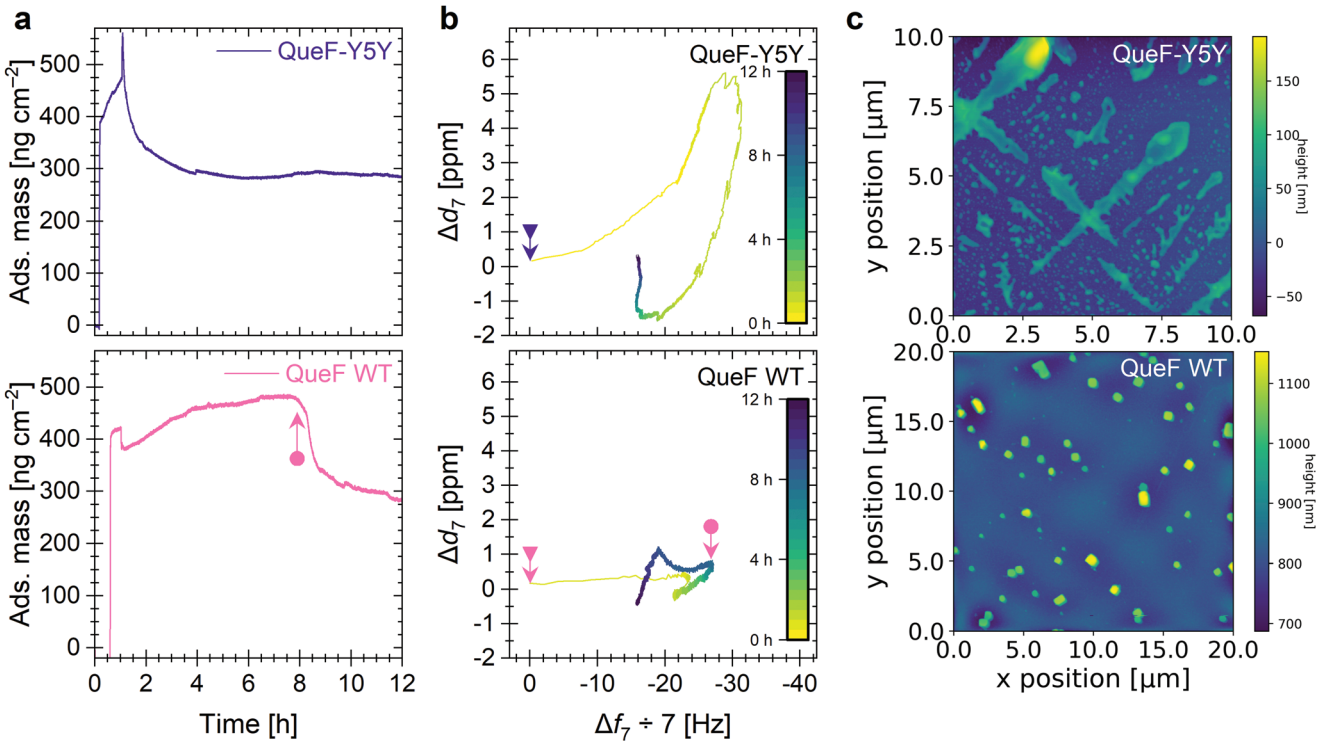

Figure 6. Quartz crystal microbalance (QCM) and AFM analysis of adsorption of QueF on graphene-coated QCM sensors. a) Hydrated mass of adsorbed protein assuming a rigid adlayer, b) evolution of adlayer structure over 12 h visualized as dissipation change compared to frequency change, c) AFM height map of the QCM sensor surface after protein adsorption. Triangles indicate the start of protein adsorption. Circles indicate the start of layer reorganization for QueF WT.

graphite tape was then placed onto a ≈1 cm^2 silicon wafer (previously cleaned in isopropanol and dried at 200 °C from 20 min.) and heated at 70 °C for 10 s to transfer the graphite from the tape to the silicon wafer. One hundred microliters of QueF protein (500 nM) was incubated onto graphite flake for 1 h in a humidity chamber at room temperature. The sample was dried in a stream of N_2 gas then placed in a vacuum desiccator overnight. AFM was run in non-contact mode. 5 and 2 µm scan areas were used for all samples with 512 lines.

Sensor Construction: Graphene grown by a chemical vapor deposition was transferred on a Si wafer with a 300 nm-thick oxidized layer and processed with a conventional lithography technique to fabricate microelectrodes. Ti/Au contacts were patterned as the source and drain electrodes. Each GFET sensor contained seven channels with individual source and drain electrodes and a common liquid reference electrode (Ag|AgCl). The graphene channel was 10 and 30 µm in length and width, respectively. Raman analysis of the GFET surface (Figure S9, Supporting Information, Isoplane 320, Teledyne Princeton Instruments, 532 nm excitation) showed characteristics of bilayer graphene ($I_{2D}/I_G = 1.3$, $\nu_{2d} - \nu_G = 1082$ cm^{-1}) with a crystallite size (L_a) of ca. 0.11 µm ($I_D/I_G = 0.17$).[48]

Measurements: The sensors were inspected for defects by visible-light microscopy and V_g sweeps (0–700 mV) to ensure sufficient conductivity in 1 mM phosphate buffer. Protein (50 µL of 500 nM) with the His_6 moiety still present was added to the GFET (500 mV V_g and 5 mV V_{sd}) and incubated for 1 h at room temperature to allow for immobilization onto graphene. i_{sd} was allowed to stabilize for 15–40 min. Reagents were added by withdrawing 25 µL of the contents of the GFET cell, replacing it was 25 µL of the reagent solution and repeating once. NADPH (50 µL of 4 µM) in 1 mM phosphate buffer was added to the cell and incubated for 30 min, then nitriles were added from stock solutions in 1 mM phosphate buffer. i_{sd} was sampled every 0.5 s.

Curve Fitting and Statistical Analysis: Currents were normalized to the signal taken before the first nitrile addition, $i_{sd}(0)$. Data were fit to Equation 1 in Origin 2020:

$$\Delta R_{sd}(c) = \frac{i_{sd}(c)}{i_{sd}(0)} = \left(\frac{i_{sd}(\infty)}{i_{sd}(0)} - 1\right)\frac{c}{K_d + c} + 1 = \Delta R_{sd}(\infty)\frac{c}{K_d + c} + 1 \quad (1)$$

where c is analyte concentration; $i_{sd}(c)$ and $i_{sd}(\infty)$ the GFET's source–drain current at a specified or infinite substrate concentration, respectively; $\Delta R_{sd}(\infty)$ is the extrapolated relative current response at infinite substrate concentration; and K_d is the dissociation constant in the same concentration units at the analyte concentration.

Error bars represent deviation among different graphene channels on the same device and so all the time points are collected simultaneously. Number of graphene channels used in each device is shown in Table 1. Error bars shown in Figure 3c represent the standard deviation calculated from the pooled variance of the measurements over 1 min. and was calculated in Excel.

Quartz Crystal Microbalance (QCM) with Dissipation Analysis: QCM measurements were carried out on QSense E1 (Biolin Scientific) using SiO_2-coated AT-cut α-quartz resonators with a fundamental frequency of (4.95 ± 0.05) MHz (QSX 303, Biolin Scientific). The resonator was exposed to UV-ozone for 10 min, rinsed with ethanol and deionized water, then dried in a stream of dry N_2 gas. Easy Transfer monolayer CVD graphene (Graphenea) was transferred to the QCM sensor using the manufacturer's protocol. The graphene sample was placed in water to detach the sacrificial layer leaving an exposed floating CVD graphene layer. The graphene layer was then transferred to onto SiO_2-coated sensor surface by using tweezers to scoop up the floating graphene layer at a 45° angle. The chip was then placed at room temperature for 30 min followed by heating at 50 °C for 1 h on a hot plate. The graphene-coated sensor was placed in a N_2 glovebox overnight then placed in 50 °C acetone bath for 1 h followed by 2-propanol bath for 1 h. Raman analysis of the graphene on the sensor (Figure S8c, Supporting Information, Renishaw inVia, 532 nm) shows spectra closely comparable to those from the GFET sensors ($I_{2D}/I_G = 1.5$–1.7, $\nu_{2D} - \nu_G = 1093$ cm^{-1},

© 2022 The Authors. Advanced Functional Materials published by Wiley-VCH GmbH

I_D/I_G = ≤0.06). The spectra also showed a broad peak at ca. 2450 cm^{-1} attributed to the underlying silica. AFM shows some species trapped between the graphene and the original sensor surface (Figure 6c) because graphene annealing requires a higher temperature (150 °C) than is recommended for the QCM-D sensors.

The graphene-coated sensor was loaded into a flow module (QFM 401) through which buffer was drawn through at 1 mL min^{-1} by peristaltic pump followed by the protein. The cell was maintained within 2 mK of 25 °C with the incorporated Peltier cooler. QSoft (v2.5.21) was used to acquire the frequency and dissipation changes for odd harmonics up to 13 after a ≈30 min. equilibration.

Adlayer mass was calculated using the Sauerbrey equation, which assumes a rigid adlayer, and a fit to a Voigt viscoelastic model. The Sauerbrey analysis used the 7th harmonic because of its moderate penetration depth and low sensitivity to mounting effects and a Sauerbrey constant of 125.3 ng cm^{-2} Hz^{-1} (= 17.9 ng cm^{-2} Hz^{-1} for the fundamental frequency).[49,50] Viscoelastic fits used the frequency and dissipation responses from harmonics 3, 5, 7, and 9, employing the chi squared minimization algorithm in QTools v3.1.24.301, constraining the shear modulus to between 10^4 and 10^8 Pa and viscosity to between 10^{-4} and 10^{-1} Pa s. Dissipation changes were small enough (<≈6 ppm) that the simpler rigid-layer approximation was within 5% of the adlayer mass calculated from viscoelastic modeling.

The maximum dry mass densities of QueF monolayers were estimated from the crystal structure of a monomer of QueF from *Vibrio cholerae* (PDB: 4GHM, dimer sequence mass = 65.9 kDa). The monomer had an approximate shape of a half ellipsoid 3.7 nm high with a base 6.6 nm × 3.2 nm. The density of a saturated monolayer with the ellipsoid base (i.e., the interface in the homodimer) on the surface is 299 ng cm^{-2}. Saturated monolayers in which the protein's long axis is parallel to the surface normal (i.e., a footprint ca. 3.7 nm × 3.7 nm) would have a dry density of 549 ng cm^{-2}.

Density Functional Theory Model Construction: A DFT active site cluster model cluster model consisting of 8205 atoms was created using previously described procedures that are based on the first and second coordination sphere of the catalytic center.[51,52] The model was created from the active site of the crystal structure coordinates of wild-type QueF (PDB: 3UXJ) with the BnCN substrate and NADPH co-factor docked in. The .pdb is a tetramer consisting of two homodimeric subunits; the model was based on chain A. The model was protonated by PropKA software to pH 7 and optimized in Gaussian-09. All residues were taken in their natural protonation state at pH 7 apart from Glu234 that was deprotonated. The model was visualized and analyzed in Chemcraft 1.8. The complete protein structure consists of 8205 atoms; however, residues not involved in catalysis were removed and a truncated model was created of a total of 263 atoms. The model consisted of only the following amino acid residues close to the active site: Trp62, Leu92, Ile93, Glu94, Ser95, Cys194, Leu195, Ile196, Thr197, Asn198, Gln199, Asp201, Phe232, His233, and Glu234 alongside. Calculations were performed at the B3LYP DFT level using 6–31 g basis set for initial geometry optimization, frequency, and scans and then followed up by a single point geometry calculation using 6–311+G(2d,2p) with Scrf = (cpcm,solvent = chlorobenzene).

Supporting Information

Supporting Information is available from the Wiley Online Library or from the author.

Acknowledgements

The authors acknowledge the UK's Biotechnology and Biological Sciences Research Council (BBSRC) for funding A.A.'s studentship (BB/M011208/1), the UK's Higher Education Funding Council for England (HEFCE) N8 Research Partnership Catalyst fund for proof-of-concept work, Dr Robin Curtis for assistance with light scattering methods, Ms. Emma-Jayne Keevill for assistance with mass spectrometry, Dr Hai Anh Le Phuong for assistance purifying $preQ_0$, and Mr. Chisyu Homma for providing representative Raman data for the GFET sensors.

Conflict of Interest

The authors declare no conflict of interest.

Author Contributions

A.A. and R.S.H. designed the enzyme and performed protein synthesis fusion. A.A., T.K., Ma. T., and M.O. produced plasmid and enzyme, and performed purification of protein. A.A., H.N., and Mi.T. probed AFM and GFET. A.A. and C.C. performed molecular dynamics. A.A., Q.E.M., and S.d.V. performed density functional theory. Y.H., S.d.V., and C.F.B. conceptualized the study. A.A. wrote the original draft. A.A., Y.H., S.d.V., and C.F.B. reviewed and edited the final manuscript.

Data Availability Statement

The data that support the findings of this study are openly available in Figshare at https://figshare.com/s/d1e5584f01aa9a7da049, reference number 33.

Keywords

2D materials, biosensing, computational chemistry, enzyme engineering, fibroin

Received: July 14, 2022
Revised: August 11, 2022
Published online:

[1] W. Gao, S. Emaminejad, H. Y. Y. Nyein, S. Challa, K. Chen, A. Peck, H. M. Fahad, H. Ota, H. Shiraki, D. Kiriya, D. H. Lien, G. A. Brooks, R. W. Davis, A. Javey, *Nature* **2016**, *529*, 509.
[2] K. Birmingham, V. Gradinaru, P. Anikeeva, W. M. Grill, V. Pikov, B. McLaughlin, P. Pasricha, D. Weber, K. Ludwig, K. Famm, *Nat. Rev. Drug Discov.* **2014**, *13*, 399.
[3] D. Li, Z. G. Shao, Q. Hao, H. Zhao, *J. Appl. Phys.* **2014**, *115*, 233701.
[4] L. S. Wong, F. Khan, J. Micklefield, *Chem. Rev.* **2009**, *109*, 4025.
[5] M. Donnelly, D. Mao, J. Park, G. Xu, *J. Phys. D: Appl. Phys.* **2018**, *51*, 493001.
[6] H. Huang, S. Su, N. Wu, H. Wan, S. Wan, H. Bi, L. Sun, *Front. Chem.* **2019**, *7*, 399.
[7] S. Islam, S. Shukla, V. K. Bajpai, Y. K. Han, Y. S. Huh, A. Ghosh, S. Gandhi, *Sci. Rep.* **2019**, *9*, 276.
[8] H. H. Bay, R. Vo, X. Dai, H. H. Hsu, Z. Mo, S. Cao, W. Li, F. G. Omenetto, X. Jiang, *Nano Lett.* **2019**, *19*, 2620.
[9] D. Kwong Hong Tsang, T. J. Lieberthal, C. Watts, I. E. Dunlop, S. Ramadan, A. E. del Rio Hernandez, N. Klein, *Sci. Rep.* **2019**, *9*, 13946.
[10] D. Kong, X. Wang, C. Gu, M. Guo, Y. Wang, Z. Ai, S. Zhang, Y. Chen, W. Liu, Y. Wu, C. Dai, Q. Guo, D. Qu, Z. Zhu, Y. Xie, Y. Liu, D. Wei, *J. Am. Chem. Soc.* **2021**, *143*, 17004.
[11] G. Seo, G. Lee, M. J. Kim, S.-H. Baek, M. Choi, K. B. Ku, C.-S. Lee, S. Jun, D. Park, H. G. Kim, S.-J. Kim, J.-O. Lee, B. T. Kim, E. C. Park, S. Il Kim, *ACS Nano* **2020**, *14*, 5135.

© 2022 The Authors. Advanced Functional Materials published by Wiley-VCH GmbH

[12] H. B. Cutter, M. Taras, *Ind. Eng. Chem., Anal. Ed.* **1941**, *13*, 830.
[13] Y. Sun, Z. Li, X. Huang, D. Zhang, X. Zou, J. Shi, X. Zhai, C. Jiang, X. Wei, T. Liu, *Biosens. Bioelectron.* **2019**, *145*, 111672.
[14] I. Lysyj, *Anal. Chem.* **1960**, *32*, 771.
[15] T. Gerasinova, A. Novikov, S. Osswald, A. Yanenko, *Eng. Life Sci.* **2004**, *4*, 543.
[16] S. S. M. Hassan, S. A. M. Marzouk, H. E. M. Sayour, *Talanta* **2003**, *59*, 1237.
[17] D. Baud, N. Ladkau, T. S. Moody, J. M. Ward, H. C. Hailes, *Chem. Commun.* **2015**, *51*, 17225.
[18] V. Lambrix, M. Reichelt, T. Mitchell-Olds, D. J. Kliebenstein, J. Gershenzon, *Plant Cell* **2001**, *13*, 2793.
[19] S. Kugimiya, T. Shimoda, J. Tabata, J. Takabayashi, *J. Chem. Ecol.* **2010**, *36*, 620.
[20] M. W. Aktar, D. Sengupta, A. Chowdhury, *Interdiscip. Toxicol.* **2009**, *2*, 1.
[21] J. R. Dunn, in *Encyclopedia of Materials: Science and Technology*, 2nd ed. (Eds: K.H. Jürgen Buschow, R. W. Cahn, M. C. Flemings, B. Ilschner, E. J. Kramer, S. Mahajan, P. Veyssière), Elsevier, Oxford, UK **2001**, p. 6163.
[22] B. Wilding, M. Winkler, B. Petschacher, R. Kratzer, S. Egger, G. Steinkellner, A. Lyskowski, B. Nidetzky, K. Gruber, N. Klempier, *Chem. - Eur. J.* **2013**, *19*, 7007.
[23] H. Seelajaroen, A. Bakandritsos, M. Otyepka, R. Zbořil, N. S. Sariciftci, *ACS Appl. Mater. Interfaces* **2020**, *12*, 250.
[24] L. Zhou, H. Mao, C. Wu, L. Tang, Z. Wu, H. Sun, H. Zhang, H. Zhou, C. Jia, Q. Jin, X. Chen, J. Zhao, *Biosens. Bioelectron.* **2017**, *87*, 701.
[25] W. Fu, L. Jiang, E. P. van Geest, L. M. C. Lima, G. F. Schneider, W. Fu, L. Jiang, E. P. van Geest, L. M. C. Lima, G. F. Schneider, *Adv. Mater.* **2017**, *29*, 1603610.
[26] V. Georgakilas, M. Otyepka, A. B. Bourlinos, V. Chandra, N. Kim, K. C. Kemp, P. Hobza, R. Zboril, K. S. Kim, *Chem. Rev.* **2012**, *112*, 6156.
[27] B. M. Brena, F. Batista-Viera, in *Immobilization of Enzymes and Cells* (Ed: J. M. Guisan), Humana Press, Berlin, **2006**, p. 15.
[28] J. Cappello, J. Crissman, M. Dorman, M. Mikolajczak, G. Textor, M. Marquet, F. Ferrari, *Biotechnol. Prog.* **1990**, *6*, 198.
[29] H. A. Klok, A. Rösler, G. Götz, E. Mena-Osteritz, P. Bäuerle, *Org. Biomol. Chem.* **2004**, *2*, 3541.
[30] P. Li, K. Sakuma, S. Tsuchiya, L. Sun, Y. Hayamizu, *ACS Appl. Mater. Interfaces* **2019**, *11*, 20670.
[31] Y. Hayamizu, C. R. So, S. Dag, T. S. Page, D. Starkebaum, M. Sarikaya, *Sci. Rep.* **2016**, *6*, 33778.
[32] L. Sun, P. Li, T. Seki, S. Tsuchiya, K. Yatsu, T. Narimatsu, M. Sarikaya, Y. Hayamizu, *Langmuir* **2021**, *37*, 8696.
[33] T. Kacar, M. T. Zin, C. So, B. Wilson, H. Ma, N. Gul-Karaguler, A. K. Y. Jen, M. Sarikaya, C. Tamerler, *Biotechnol. Bioeng.* **2009**, *103*, 696.
[34] D. Khatayevich, T. Page, C. Gresswell, Y. Hayamizu, W. Grady, M. Sarikaya, *Small* **2014**, *10*, 1505.
[35] J. Jung, B. Nidetzky, *J. Biol. Chem.* **2018**, *293*, 3720.
[36] J. Yang, R. Yan, A. Roy, D. Xu, J. Poisson, Y. Zhang, *Nat. Methods* **2014**, *12*, 7.
[37] A. J. M. Ribeiro, L. Yang, M. J. Ramos, P. A. Fernandes, Z.-X. Liang, H. Hirao, *ACS Catal.* **2015**, *5*, 3740.
[38] A. J. M. Ribeiro, L. Yang, M. J. Ramos, P. A. Fernandes, Z.-X. Liang, H. Hirao, *ACS Catal.* **2015**, *5*, 3740.
[39] Y. Kim, M. Zhou, S. Moy, J. Morales, M. A. Cunningham, A. Joachimiak, *J. Mol. Biol.* **2010**, *404*, 127.
[40] L. Yang, S. L. Koh, P. W. Sutton, Z. X. Liang, *Catal. Sci. Technol.* **2014**, *4*, 2871.
[41] S. Verma, R. Dixit, K. C. Pandey, *Front. Pharmacol.* **2016**, *7*, 107.
[42] M. G. Quesne, R. A. Ward, S. P. de Visser, *Front. Chem.* **2013**, *1*, 39.
[43] T. P. McNamara, C. F. Blanford, *Analyst* **2016**, *141*, 2911.
[44] F. Caruso, D. N. Furlong, P. Kingshott, *J. Colloid Interface Sci.* **1997**, *186*, 129.
[45] F. Höök, M. Rodahl, B. Kasemo, P. Brzezinski, *Proc. Natl. Acad. Sci. U.S.A* **1998**, *95*, 12271.
[46] K. Noge, S. Tamogami, *FEBS Lett.* **2013**, *587*, 1811.
[47] W. Fu, T. F. Van Dijkman, L. M. C. Lima, F. Jiang, G. F. Schneider, E. Bouwman, *Nano Lett.* **2017**, *17*, 7980.
[48] A. C. Ferrari, *Solid State Commun.* **2007**, *143*, 47.
[49] F. Fei, A. Gallas, Y. C. Chang, Y. Rao, A. C. Hunter, R. E. P. Winpenny, A. L. Herrick, N. P. Lockyer, C. F. Blanford, *ACS Appl. Mater. Interfaces* **2017**, *9*, 27544.
[50] K. Singh, C. F. Blanford, *ChemCatChem* **2014**, *6*, 921.
[51] N. J. Fowler, C. F. Blanford, J. Warwicker, S. P. de Visser, *Chem. - Eur. J.* **2017**, *23*, 15436.
[52] M. Q. E. Mubarak, E. F. Gérard, C. F. Blanford, S. Hay, S. P. De Visser, *ACS Catal.* **2020**, *10*, 14067.
[53] A. A. Mohamed, H. Noguchi, M. Tsukiiwa, C. Chen, R. S. Heath, M. Q. E. Mubarak, T. Komikawa, M. Tanaka, M. Okochi, S. P. de Visser, Y. Hayamizu, C. F. Blanford, A GFET nitrile sensor using a graphene-binding fusion protein, **2022**, https://figshare.com/s/d1e5584f01aa9a7da049.

© 2022 The Authors. Advanced Functional Materials published by Wiley-VCH GmbH